Chapter 3

Magnetic and electric properties of Ni-doped ZnO nanoparticles exhibit diluted magnetic semiconductor in nature

3.1. Introduction:

The potential applications of DMS in spintronics have catapulted the incredible attention of researchers in these materials [190-193]. Coupling between the electron charge and degrees of freedom of spin are a significant requirement for spintronic devices. Magnetic ordering at suitable temperature is the basic need for such relevance. The incorporation of transition metals in semiconductor like ZnO with wide band gap is expected to create ferromagnetic ordering at normal temperature, originated from carrier mediated exchange interaction. Though several studies have been done on Mn-doped ZnO yet very few literatures described on Ni-doped ZnO.

Hexagonal wurtzite ZnO possesses tetrahedrally coordinated O^{2-} and Zn^{2+} ions, assembled along the c-axis with alternating pattern. Also, ZnO contains large exciton binding energy of magnitude 60 meV and therefore it is potential candidate as a phosphor material with UV light emission [194, 195]. The comparatively smaller diameter of Ni^{2+} ion with tetrahedral coordination is expected to have a better solubility in host ZnO. However, there have been conflicting reports in the literature. Thus an interest have grown to investigate the Ni-doped ZnO nanomaterials with doping concentrations 3, 6, 9, 12 and 15% to explore the potentiality of magnetoelectric coupling in the samples.

The Ni-doped ZnO nanopowders have been synthesized through chemical precipitation technique with adding together acetate salts and tetramethylammonium hydroxide simultaneously. The calcined nanopowders have been characterized by XRD, TEM, FTIR, UV-Vis absorption and FL for structural, elemental analysis and optical properties respectively. The dielectric, ferroelectric, SQUID and ME coupling measurements were carried out for the electric, magnetic characterization and to assess the magnetoelectric coupling in the samples.

3.2. Experimental:

The nanocrystalline $Zn_{1-x}Ni_xO$ (x = 0.00, 0.03, 0.06, 0.09, 0.12, 0.15) samples were synthesized through simple chemical precipitation process. Zinc acetate dihydrate [$Zn(CH_3CO_2)_2 \cdot 2H_2O$; ≥98% Sigma Aldrich], nickel acetate tetrahydrate [$Ni(CH_3CO_2)_2 \cdot 4H_2O$; ≥99% Sigma Aldrich] and tetramethylammonium hydroxide [$N(Me)_4OH.\ 5H_2O$] (25% in water) were used as precursor materials. Solutions of 0.5 M acetates were made using double distilled water as solvent under constant stirring condition by a magnetic stirrer. To synthesize $Zn_{1-x}Ni_xO$, initially 0.5 ml $N(Me)_4OH.\ 5H_2O$ was mixed to 140 ml distilled water and during this process the temperature was maintained at 80 ^{o}C. Then metal acetates of 20 ml 0.5 M stoichiometric ratio (Zn^{2+}:Ni^{2+} = $1-x$: x) were added gradually into the beaker. First the synthesis temperature was maintained at 50-70 ^{o}C for 2 hours but complete precipitation could not be achieved indicating that the reaction is not achieving completion and is very slow at this temperature. The reaction temperature was then increased to 80 ^{o}C and maintained for 2 hour with constant stirring. We obtained the desired precipitates of nanosized particles. The temperature and the time are set in such a way as to maintain a higher reaction rate and allowing the reaction to achieve completion respectively. The formation of the compound is checked by X-ray diffraction. The precipitated particles were centrifuged for 5 minutes at 9500 rpm. This process was repeated for 5 times using ethanol and double distilled water to wipe off the insignificant amount of probable ingredients $Ni(OH)_2$ and any unreacted component. The precipitated particles were dried at 150 ^{o}C and calcined at 500 ^{o}C for 2 hour in air atmosphere to form nanopowders. The calcined materials were finally compressed into pellets and the pellets were sintered at 600 ^{o}C for 3 hour for electrical characterizations. The flow chart of synthesis process is given below.

- **Flow chart of synthesis process:**

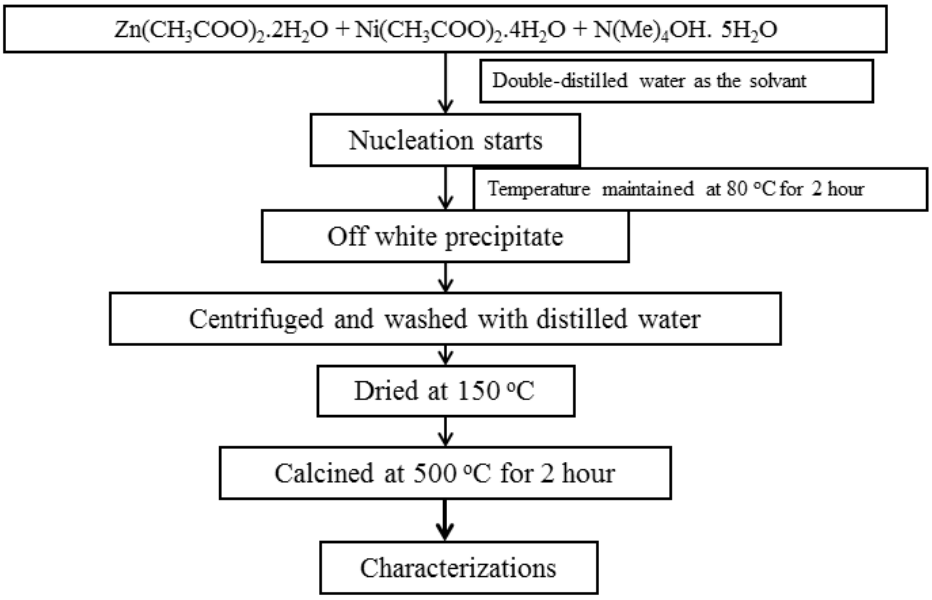

Structural, optical, electrical and magnetic property of the Ni-doped ZnO nanoparticles have been investigated through XRD, TEM, FTIR, UV-Vis absorption, FL, dielectric, P-E, ME coupling and SQUID measurements as discussed in sec 2.2 of chapter 2.

3.3. Results and discussions:

3.3.1. EDX and XRD characterizations:

The elemental compositions of the nanoparticles are tested by EDX study. The EDX spectra of two samples, $Zn_{0.94}Ni_{0.06}O$ and $Zn_{0.91}Ni_{0.09}O$, are displayed in figure 3.1(a) and 3.1(b) respectively. The spectra of these samples indicate the presence of Zn, Ni, O, C and Cu. The presence of the peaks belonging to C and Cu have their origin in the carbon coated copper grid. Thus from EDX study it is confirmed that there is no impurity in the nanoparticles. Table-I presents the weight and atomic ratio of the elements as obtained by EDX spectroscopy. Ni to (Zn+Ni) ratio in the two samples is found to be 0.0653 and 0.0927 which is nearly the predicted values of 0.06 and 0.09 respectively. The structure and phase purity of all the prepared nanoparticles have been assessed through the most reliable X-ray diffraction study.

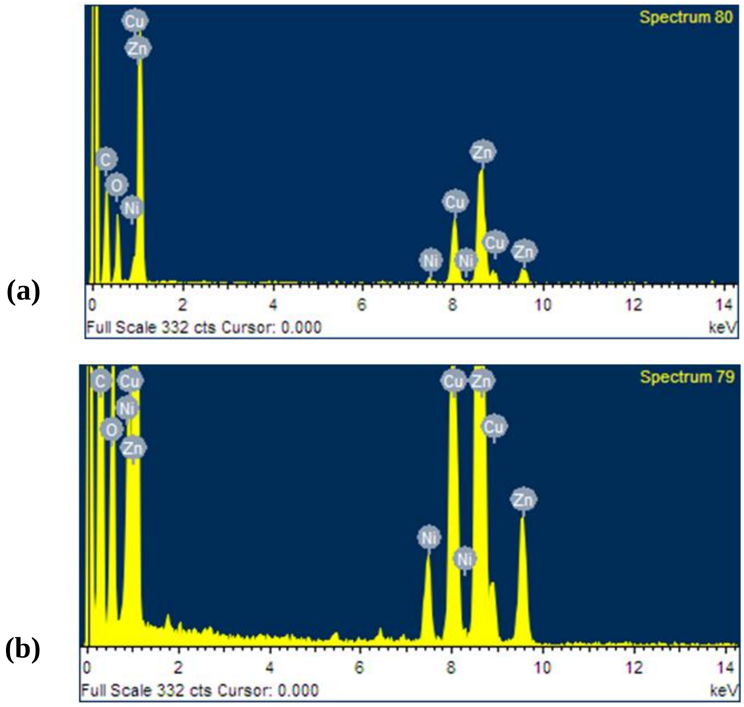

Fig. 3.1. EDX spectra of **(a)** $Zn_{0.94}Ni_{0.06}O$ and **(b)** $Zn_{0.91}Ni_{0.09}O$ samples.

Table-I. Wt%, At% and elemental atomic ratio of Ni-doped ZnO nanoparticles.

	$Zn_{0.94}Ni_{0.06}O$				$Zn_{0.91}Ni_{0.09}O$			
Element	Wt%	At%	Elemental Atomic Ratio E/(Zn+Ni)	Expected ratio	Wt%	At%	Elemental Atomic Ratio E/(Zn+Ni)	Expected ratio
O	13.92	20.98	1.4889993	1.00	10.77	12.72	1.473928	1.00
Ni	2.24	0.92	0.0652945	0.06	2.47	0.80	0.0927	0.09
Zn	35.70	13.17	0.9347055	0.94	27.08	7.83	0.9073	0.91

The X-ray diffraction patterns of $Zn_{1-x}Ni_xO$ nanoparticles for different concentrations are exhibited in figure 3.2. The 2θ positions relating to the noticed peaks of XRD spectra for all the pure and doped compounds have been stated in table-II. All the peaks listed in the JCPDS 36-1451 file corresponding to hexagonal wurtzite structure [196, 197] of ZnO is found to tally with the XRD pattern of the sintered powders of pure ZnO and those of the Ni-doped samples with chemical formula $Zn_{1-x}Ni_xO$ (x = 0.03, 0.06, 0.09, 0.12 and 0.15). However, an extra small diffraction peak at around 43^o is observed in the XRD patterns of the doped samples with $x \geq 0.06$.

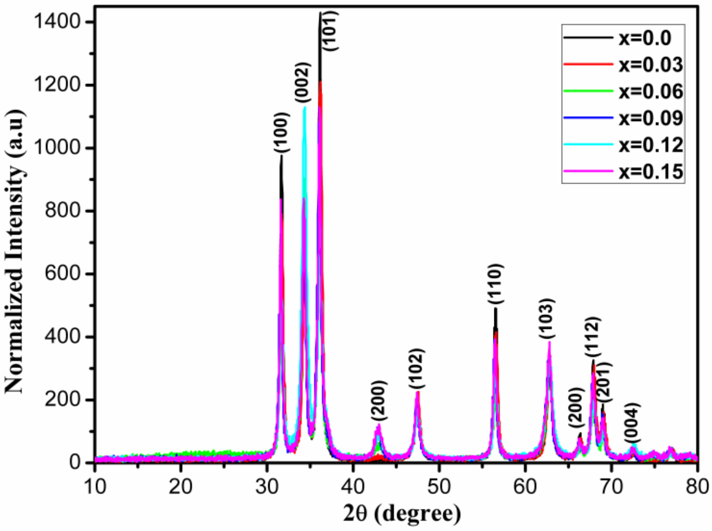

Fig. 3.2. XRD spectra of $Zn_{1-x}Ni_xO$.

Table-II. The 2θ for the observed peaks in the XRD spectra of $Zn_{1-x}Ni_xO$.

Plane index (hkl)	Observed diffraction angle 2θ (degree) of $Zn_{1-x}Ni_xO$					
	x = 0.00	x = 0.03	x = 0.06	x = 0.09	x = 0.12	x = 0.15
100	31.682	31.713	31.625	31.578	31.694	31.631
002	34.325	34.370	34.290	34.240	34.348	34.289
101	36.152	36.191	36.108	36.058	36.171	36.112
*	–	–	42.988	42.871	42.991	42.945
102	47.470	47.500	47.422	47.387	47.490	47.431
110	56.546	56.571	56.507	56.447	56.552	56.493
103	62.818	62.857	62.774	62.706	62.812	62.745

*NiO (200) peak

It is realized from the table-II that the diffraction angle related to all the peaks of $Zn_{0.97}Ni_{0.03}O$ is slightly higher than the diffraction angle of the consequent peaks of ZnO. Both the lattice parameters a and c for $Zn_{0.97}Ni_{0.03}O$ nanoparticles decrease as compared to those of ZnO. The decrement of the lattice parameters might be attributed to the substitution of comparatively smaller size of Ni^{2+} ion in place of the tetrahedral Zn^{2+} sites of ZnO matrix. It is worth mention here that the ionic radius of Ni^{2+} in tetrahedral coordination is 69 pm and is smaller than the ionic radius of Zn^{2+} ions (74 pm). The additional small diffraction peak at around 43^o in the samples with higher doping concentration of Ni ($x \geq 0.06$) indicates the presence of a secondary phase. It is imperative to find the origin of this extra peak. EDX spectra confirm the impossibility of any impurity in the nanomaterials. So, we have to search for the coming of secondary phase related to metallic Ni or NiO. Metallic Ni and its oxide NiO cystallize in fcc. As evident from the JCPDS 01-1239 file, Ni exhibit X-ray diffraction peaks at angle of 44.7^o and 54.5^o corresponding to (111) and (200) plane respectively. The JCPDS 73-1519 file related to NiO displays X-ray diffraction peak at angle of 37.11^o (111) and 43.3^o (200) with octahedral coordination for both Ni^{2+} and O^{2-}. As any peak near 44.7^o and 54.5^o is not revealed in the XRD spectra of the synthesized nanosamples, the presence of Ni phase is ruled out. However, the presence of a small peak like anomaly nearly at 37^o overlapped by the (101) peak of ZnNiO. A peak at around 43^o as exhibited in the XRD pattern in points to the presence of a small secondary NiO phase in addition to the hexagonal wurtzite phase of ZnNiO in the nanopowders for $x \geq 0.06$. The diffraction angle of all the peaks for concentrations $x = 0.06$ and 0.09 decreases which specify increment of the lattice parameters a and c. It is worthy informed that NiO crystallizes in rocksalt phase with octahedral coordination wherein the radius of Ni^{2+} ions is 83 pm, which is relatively higher than Zn^{2+} ions (74 pm) in the host lattice. Therefore the increase in lattice parameters can be discussed depending on the presence of the secondary NiO phase and increased Ni^{2+} ion size in octahedral coordination. The peak intensity related to the NiO phase increases from 0.049 to 0.104 for concentration $x = 0.06$ to 0.09. The interplanar spacing for NiO (200) also increases with increasing x (except for $x = 0.12$) specifying larger space to NiO ions. However, it is observed that for $x = 0.12$, the peak intensity of the NiO phase decreases and the peaks shift towards right as a consequence of the diffraction angle as well as a decrease in the lattice parameters. The unexpected increase of diffraction angle and decrease of lattice parameters for $x = 0.12$ might be the consequence of strain relaxation.

Table-III depicts the cell parameters, c/a ratio and the degree of distortion from ideal hexagonal wurtzite structure (R), cell volume, the coherently diffracted domain size and the lattice strain produced in the nanoparticles of all the compositions.

Any type of distortion from the ideal hexagonal wurtzite structure is identified through a parameter $R=\sqrt{\frac{8}{3}}\frac{a}{c}$. As can be noticed from the table-III the degree of distortion, R has value very near to the ideal value of 1.0 for all the prepared compositions. The lattice strain (ε) and the coherently diffracted domain (crystallite) size (D) were determined from the intercept and slope of the curve of $\beta cos\theta$ vs. $4sin\theta$ by using Williamson–Hall relation: $\beta Cos\theta=\varepsilon 4\sin\theta+\frac{k\lambda}{D}$, where, β = FWHM (Full-Width at Half Maxima) of the diffraction peak and λ = wavelength of Cu-K_α radiation (1.5418 Å). For the nanoparticles with x = 0.03, with the replacement of Zn^{2+} by the smaller Ni^{2+} in place of the tetrahedral sites produces slightly higher values of the degree of distortion with increase in the lattice strain. In case of x = 0.06, a portion of the Ni^{2+} ions reside in tetrahedral sites by replacing the Zn^{2+} ions and a small portion occupy octahedral sites having larger ionic radius. So the degree of distortion decreases and the lattice strain is found to be the lowest among all the studied samples. For x = 0.09, the lattice strain increases with increase in number of Ni^{2+} ions reside in the octahedral sites. However, for nanoparticles with x = 0.12, the strain is found to be highly relaxed with compare to corresponding x = 0.09. For this composition the lattice parameters are also found to have smaller values compared to that of x = 0.09 denoting some anomalous behavior in the sample. The strain and the lattice parameter for the sample with x = 0.15 were found to higher values than other studied compositions.

Table-III. The lattice parameters of Ni-doped ZnO nanoparticles of studied compositions.

Molar ratio of Ni	a (Å)	c (Å)	c/a	Degree of distortion, R	cell volume (Å^3)	particle size (Å)	strain E-04	D (nm) of (002) peak
0	3.25635	5.22014	1.60307	1.01867	47.93604	224.53	7.42	20.0
0.03	3.25435	5.2145	1.60232	1.01915	47.82545	208.98	8.43	17.5
0.06	3.25861	5.22236	1.60263	1.01894	48.02302	185.76	4.64	17.3
0.09	3.2628	5.22845	1.60244	1.01906	48.20274	217.84	9.24	15.0
0.12	3.25559	5.21578	1.6021	1.01928	47.87365	171.95	4.80	12.7
0.15	3.25968	5.22252	1.60216	1.01925	48.05604	238.42	10.00	16.7

In case of $x = 0.03$ where all the Ni ions substitute the Zn ions and for $x = 0.06$, except for a few, maximum of the Ni ions substitute the Zn ions, the reaction mobility constrains the growth of surface due to higher bond energy of Ni–O (≈ 366eV) than that of Zn–O (≈ 250eV) [198] and in result decrease the crystallite size. Since the number of Ni ions increases the octahedral sites, a secondary phase is developed and crystallite size of the ZnNiO phase is increased for $x = 0.09$ and 0.15.

3.3.2. HRTEM and SAED:

The TEM characterization of $Zn_{0.94}Ni_{0.06}O$ and $Zn_{0.91}Ni_{0.09}O$ nanopowders in figure 3.3(a) and 3.3(b) vindicate the XRD findings relevant to the hexagonal wurtzite structure with grain size about 20 nm. The crystallite size of the nanoparticles presented in table-III is nearly same size as that of the order of grain exposed in the TEM photograph, approving single domain within the grain. The HRTEM photographs of the nanoparticles are exhibited in figure 3.4(a) and 3.4(b). These photographs endorse the uniform structural growth appears at the surface of the nanoparticles. The interplanar distance as has been found from the HRTEM photographs is around 0.24 nm. The interplanar distance of (101) planes in the studied nanopowders, as obtained from XRD analyses and the lattice parameters stated in table-IV is close to this value. Further, the intensity of the XRD peak corresponding to (101) set of planes is found to be most intense. These observations put (101) as the preferred growth direction of prepared samples. For ready reference, the planar spacing d_{hkl} for the (101) plane considered from XRD data $d_{hkl} = \frac{n\lambda}{2\sin\theta}$, the one determined on the basis of the well-known relation for the planar spacing related to the lattice parameters $d_{hkl} = \left[\frac{4}{3}\left(\frac{h^2+hk+k^2}{a^2}\right)+\frac{l^2}{c^2}\right]^{-\frac{1}{2}}$ and that obtained from HRTEM are displayed in table-IV.

Table-IV. Interplanar spacing of the (101) plane for 6% and 9% Ni-doped ZnO.

Compound	Plane index (hkl)	2θ	d (hkl) expt (Å)	d (hkl) calculated (Å)	d (hkl) from HRTEM (Å)
$Zn_{0.94}Ni_{0.06}O$	(101)	36.193^o	2.482	2.479	2.4
$Zn_{0.91}Ni_{0.09}O$	(101)	36.108^o	2.487	2.483	2.4

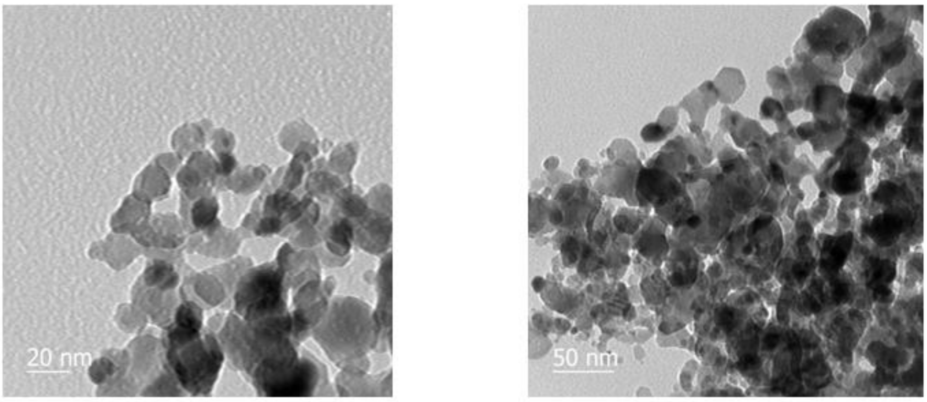

(a) **(b)**

Fig. 3.3. TEM image of **(a)** $Zn_{0.94}Ni_{0.06}O$ and **(b)** $Zn_{0.91}Ni_{0.09}O$ samples.

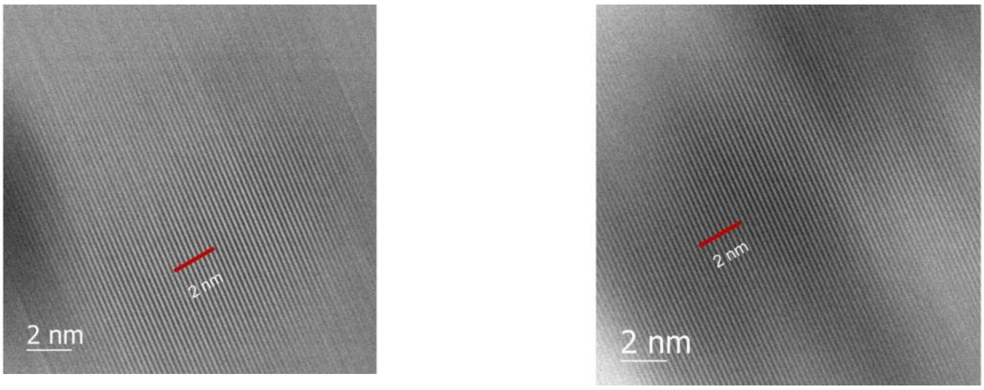

(a) **(b)**

Fig. 3.4. HRTEM image of **(a)** $Zn_{0.94}Ni_{0.06}O$ and **(b)** $Zn_{0.91}Ni_{0.09}O$ samples.

Selected area electron diffraction (SAED) patterns are exhibited in figure 3.5(a) and 3.5(b). SAED pattern represents the self-organization of nanoparticles and confirm the single crystalline nature with hexagonal pattern.

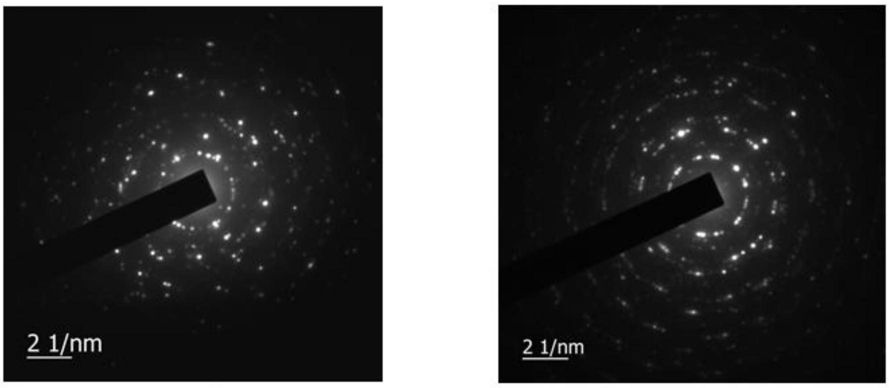

(a) **(b)**

Fig. 3.5. SAED pattern of **(a)** $Zn_{0.94}Ni_{0.06}O$ and **(b)** $Zn_{0.91}Ni_{0.09}O$ samples.

3.3.3. FTIR spectra:

FTIR is a useful technique to know about the chemical bonding among the elements present in the samples. The FTIR spectra of $Zn_{1-x}Ni_xO$ nanoparticles are exhibited in figure 3.6(a) and 3.6(b). Zn–O stretching band is the origin of strong absorption band in 399-555 cm^{-1} in pure ZnO. This band is mentioned as the superposition of consecutive three bands related to the stretching E_2 (LO) mode of Zn–O (metal-oxygen vibration) [199] and two other surface phonon modes as SPM (A_1 (TO)) and SPM (E_1 (TO)) [200]. The corresponding absorption band for $Zn_{1-x}Ni_xO$ compounds are observed at 398-589, 398-563, 398-569, 398-552 and 398-563 cm^{-1} for $x = 0.03$, 0.06, 0.09, 0.12 and 0.15 respectively. The band edge is found to be blue shifted with respect to pure ZnO for all the doped samples though the blue shift is maximum for 3% Ni-doped ZnO nanoparticles. It is worth mentioning here that all the Ni^{2+} ions for $x = 0.03$ substitute Zn^{2+} ion sites in tetrahedral coordination. A part of the Ni^{2+} ions for higher values of x, replace Zn^{2+} ion sites in octahedral coordination sites with creation of a secondary phase. E_2 (LO) stretching peak of nickel doped Zn–O vibration at 436, 440, 430, 428, 448 and 440 cm^{-1} for $x = 0$, 0.03, 0.06, 0.09, 0.12 and 0.15 respectively endorses the formation of ZnO like hexagonal wurtzite structure. While, the blue shift can be explained for $x = 0.03$ in the absorption peak as the consequence of substitution of Ni^{2+} ions at the Zn^{2+} sites with tetrahedral coordination and consequent smaller lattice parameter and smaller bond length. The red shift in the absorption peak for $x = 0.06$ and 0.09 is generated due to reside of Ni^{2+} ions in octahedral sites with larger ion size and lattice parameters as envisaged in table-III.

The absorption peak at 907-919 cm^{-1} for all the nanoparticles assigned to defect mediated Zn–O–Zn [197] and the peak around 2332-2338 cm^{-1} to the M–CO stretching [195, 201], where M stand for doped transition metal element. The intensity corresponding to M–CO peak is highly reduced for $x = 0$, 0.06 and 0.12 where the samples are most relaxed with minimal strain. Both these absorption peaks explore similar characteristics with change in concentration as have been denoted for the peak at 440 cm^{-1}. The other absorption peaks found in all the samples at 3454 cm^{-1}, 2922 cm^{-1}, 1626 cm^{-1} and 1388 cm^{-1} are usually attributed to O–H stretching mode of water [200, 202], C–H mode [203], H–O–H bending vibrations of interlayer water molecule [202, 204] and the symmetric C=O stretching vibration modes [205, 206] respectively. These peaks generally arise from the adsorbed elements through the surface of the compounds from the atmosphere.

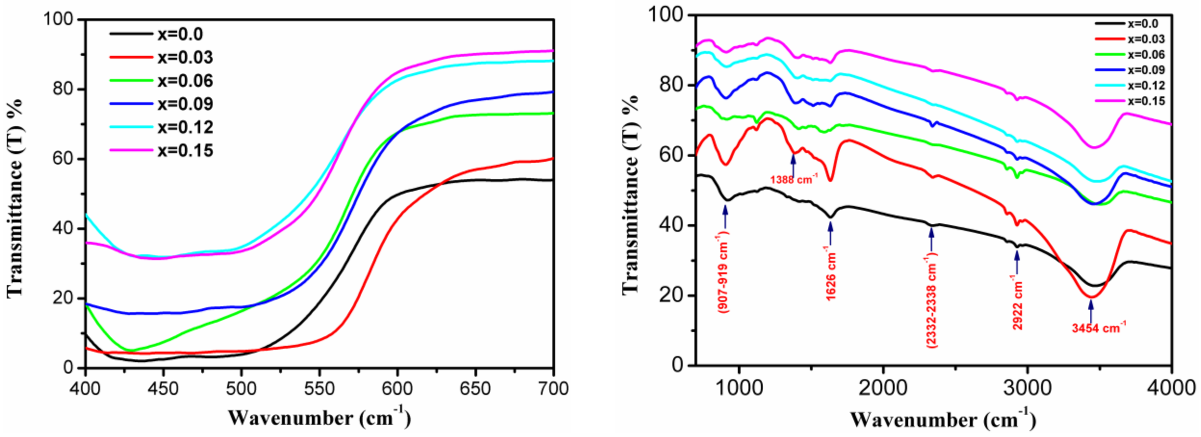

(a) **(b)**

Fig. 3.6. FTIR spectra of $Zn_{1-x}Ni_xO$ series for **(a)** 400-700 cm^{-1} and **(b)** 700-4000 cm^{-1}.

3.3.4. UV-Visible spectra:

The absorption spectra of the $Zn_{1-x}Ni_xO$ series was studied by UV-Vis spectrophotometer in the wavelength range 300-800 nm and are exhibited in figure 3.7. Normally absorbance value is reliant to several features like the distortion in grain structure, size of particles, oxygen deficiency etc. The absorption peak corresponding to exciton recombination is observed at 371 nm (3.34 eV) for pure ZnO and at 365 nm (3.40 eV), 367 nm (3.38 eV), 363 nm (3.42 eV), 357 nm (3.47 eV) and 363 nm (3.42 eV) for 3%, 6%, 9%, 12% and 15% Ni-doped ZnO nanopowders respectively [203, 207]. The excitonic peaks explore a blue shift for doped samples. This blue shift of absorption band edge can be explained according to the Moss-Burstein band filling effect [203, 208, 209]. In figure 3.7 absorption peak intensity increases with increasing doping concentration. This absorbance peak wavelength is an attribute of the intrinsic band gap of the sample and the intensity depends on the number of states at the valence band maxima. With increase in particle size, the number of states in a band increases (as number of states in a band being equal to 2 times the number of unit cells in the crystallite) and thus enhances the transition probability across the intrinsic band gap. It is worth pointing here that for the sample with $x = 0.15$, the particle size is maximum and the absorbance is also maximum among the studied samples. According to Moss-Burstein effect 15% Ni-doped ZnO nanoparticles should have lowest absorption peak wavelength but it has slightly higher absorption peak wavelength than 12% Ni-doped ZnO due to bigger crystallite size [202].

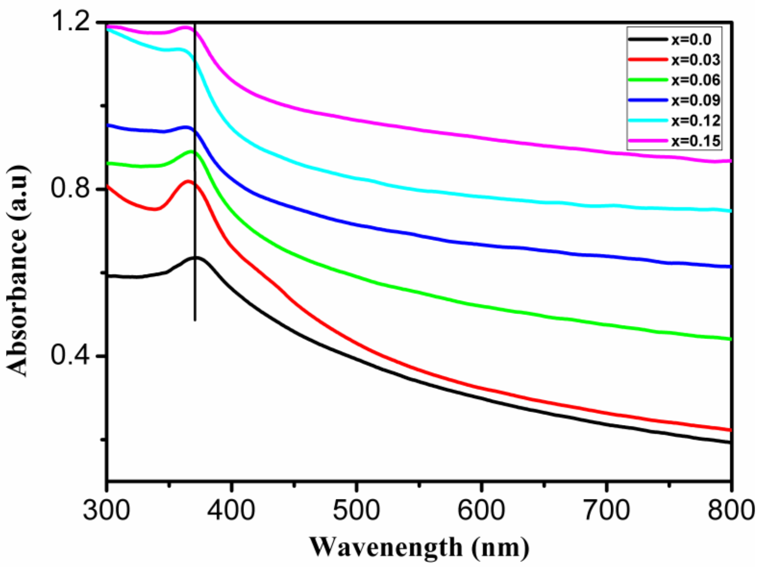

Fig. 3.7. Absorption spectra of $Zn_{1-x}Ni_xO$ series.

3.3.5. Fluorescence spectra:

The fluorescence spectra of all the $Zn_{1-x}Ni_xO$ samples studied at room temperature using high intense Xe source excited at 325 nm are displayed in figure 3.8. To detect the exact position of the peaks the spectra of the pure ZnO nanopowders is resolved into multiple Gaussian peaks and displayed as inset in figure 3.8. A suitable fit is attained for the spectra with five different Gaussian peaks. All the Ni-doped ZnO nanopowders exhibit similar peaks like pure ZnO in the FL spectra. As can be observed from the inset graph, the emission peaks are obtained at 359 nm, 397 nm, 439 nm, 490 nm and 524 nm for all the prepared samples. The emission peak of FL spectra at 359 nm (3.45 eV) and 397 nm (3.12 eV) are attributed to the radiative recombination of free exciton-exciton collision processes [210].

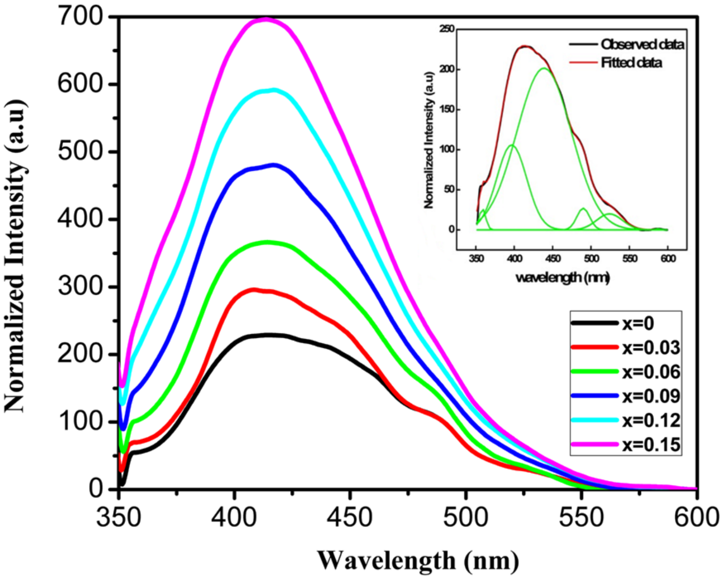

Fig. 3.8. FL spectra of $Zn_{1-x}Ni_xO$ series.

The emission peak of UV region is followed by the strong visible emission band of wavelength range 400-525 nm. Generally, visible region emissions are deep-level emissions resulting from the recombination of deeply trapped electrons in oxygen vacancies and the photo-generated holes with zinc interstitials [211-213]. As separation of the emissions by different type of defects is quite difficult, the exact source of the visible region emissions in ZnO is yet to be resolved. Zhao et al. and Fan et al. assigned the violet emission band in ZnO at around 439 nm (2.82 eV) to either of the electronic transition between the level of interstitial zinc (Zn_i) and the valence band or that between the lower part of the conduction band and the level of Zn vacancy (V_{Zn}) [214, 215]. The weak blue emission band of 490 nm (2.53 eV) is explained on the basis of intrinsic defects to the valence band [216]. However, green emission of ZnO is ascribed to defect states and oxygen vacancy (V_O) [217]. The weak green luminescence at 524 nm (2.36 eV) is originated due to the transition of photo-assisted electron from a deep level of conduction band to a deeply trapped hole from an oxygen vacancy [211, 218]. The emission intensity in the luminescence spectra of Ni-doped ZnO nanoparticles increases with increasing doping concentration as compared to that of pure ZnO nanoparticles because of the distortion developed due to Ni ion impurities within the host ZnO lattice.

3.3.6. Dielectric properties:

The complex impedance spectroscopy (CIS) has a capacity of non-destructive analysis for investigating the electric and dielectric behavior of ceramic compounds. In the complex impedance curve of the imaginary part Z'' vs. the real part Z' familiar as the Nyquist plot; the grain, grain boundary and electrode interface contribution to the polarization mechanism, manifest as consecutive semicircles. The contribution from grain boundary and electrode interface gets activated at relatively higher temperatures. The centre of a perfect semicircle on the real axis signifies an ideal Debye type nature attributing to a mono-relaxation mechanism. Such semicircular arcs are expected only in homogeneous materials and are represented through parallel RC circuit. The grain size variation and consequent distribution of the relaxation time, the semicircular arcs in the complex impedance plane relating to the grain and grain boundary effects gets tilted to the real axis with the centre generally positioned below the real axis.

As can be observed from the figure 3.9(a), complex impedance plot of undoped ZnO at room temperature comprise a single depressed semicircle implying polarization from only grain effect. However, the tilt angle of 7.62^o below the real axis indicates small distortion due to thin grain homogeneity. Two depressed semicircular arcs are attributing to grain and grain boundary effect for the doped samples $x = 0.03$ and $x = 0.09$ (figure 3.9(b) & 3.9(c)) displayed in the Nyquist plot. The grain boundary contribution in the doped compounds seems to be the consequence of the mobility of smaller Ni ion in tetrahedral coordination.

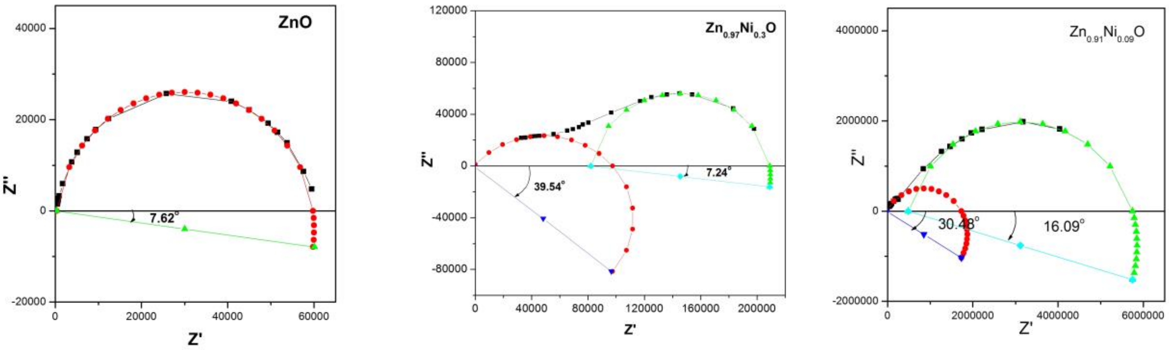

(a) **(b)** **(c)**

Fig. 3.9. Nyquist plot (complex impedance plots of the active part Z'' vs. the reactive part Z') of **(a)** pure ZnO, **(b)** $Zn_{0.97}Ni_{0.03}O$ and **(c)** $Zn_{0.91}Ni_{0.09}O$ samples.

The room temperature dielectric records of pure and Ni-modified ZnO nanocompounds with frequency 100 Hz to 100 kHz are exhibited in figure 3.10(a) and 3.10(b). The dielectric constant displays normal decreasing trend with increase in frequency except a small unusual effect in the dielectric constant of Ni-doped ZnO compounds at around 5 kHz. Again a decrement in dielectric constant is maintained with increase in doping concentration for the whole frequency range. The plots imply two different polarization mechanisms both the side of 5 kHz frequency. The high value of dielectric constant at lower frequency can be explained on the basis of Maxwell-Wagner mechanism depending on the movement of mobile ions to the grain boundary as established in the Nyquist plot. The grain boundary is more insulating in comparison to less resistive grain interior correlating with the Maxwell-Wagner mechanism. As have been found from the Nyquist curve for $x = 0.03$ the boundary and bulk resistances are 127 kΩ and 98.7 kΩ while that for $x = 0.09$, 5170 kΩ and 1755 kΩ respectively. Consequently the capacitance owing to the grain boundary possesses large value than the capacitance of the grain interior.

In figure 3.10(b), the dispersion curve of loss tangent explores low loss in the samples. The loss tangent plot possesses two influences

$$\tan\delta = \frac{\varepsilon''}{\varepsilon'} + \frac{\sigma_{dc}}{\omega\varepsilon'} \qquad (3.1)$$

The two terms in the loss tangent correspond to the Debye type dipolar relaxation mechanism and the dc conductivity [219]. The second term is prominent at low frequency region because of the term ω in the denominator and increases with decrease in frequency as observed in figure 3.10(b).

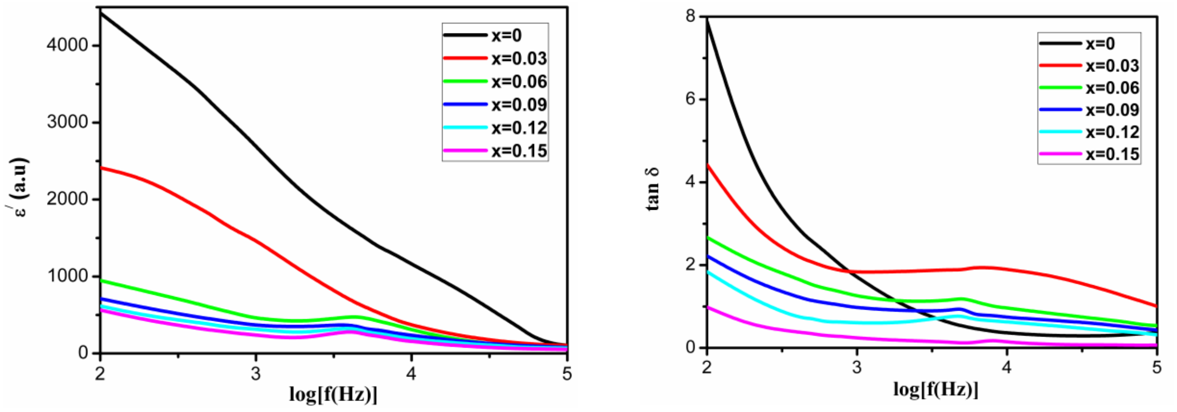

(a) **(b)**

Fig. 3.10. Variation of **(a)** dielectric constant and **(b)** loss tangent with frequency of Ni-doped ZnO.

3.3.7. Ferroelectric property:

Ferroelectric property of $Zn_{0.91}Ni_{0.09}O$ and $Zn_{0.85}Ni_{0.15}O$ has been studied at room temperature. They exhibit ferroelectric loop presented in figure 3.11. The remnant polarization values for $Zn_{0.91}Ni_{0.09}O$ and $Zn_{0.85}Ni_{0.15}O$ nanoparticles have been obtained as 9×10^{-3} and 6×10^{-3} $\mu C/cm^2$. The loop area of $Zn_{0.85}Ni_{0.15}O$ is also less than loop area of $Zn_{0.91}Ni_{0.09}O$ nanoparticles. It is worth pointing here that the secondary NiO phase increases with increasing Ni content. In the dominant wurtzite phase of $Zn_{1-x}Ni_xO$, the smaller Ni^{2+} ion at the position of Zn^{2+} ion of host ZnO produces a structural disorder along the polar *c*-axis as the dopants tend to occupy off-centered positions and develops an electric dipole moment

[29]. However, the increasing secondary phase, wherein the Ni^{2+} ion in octahedral coordination with a larger ionic radius perform as pinning centers which keep away the charge carrier from free movement across the grain boundaries and results in the decrement in remnant polarization and loop area [151]. Some reports suggest that ferroelectricity in host semiconducting substances with a non-perovskite structure can also develop through indirect interaction of impurity dipoles and free charge carriers according to the Ruderman-Kittel-Kasuya-Yosida (RKKY) mechanism [148].

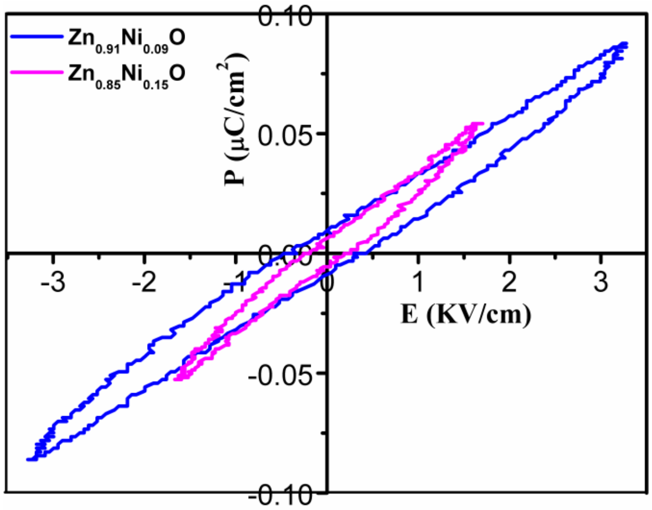

Fig. 3.11. P-E loop of $Zn_{0.91}Ni_{0.09}O$ and $Zn_{0.85}Ni_{0.15}O$ sample.

3.3.8. Magnetic property:

The variation of magnetic moment with magnetic field (M−H) of $Zn_{0.91}Ni_{0.09}O$ sample has been examined at 5K with maximum applied field ± 4 T using SQUID and the result is exhibited in figure 3.12. The figure suggest weak ferromagnetic nature of the compound at the experimental temperature [220]. ZnO nanoparticles have been reported to display room temperature diamagnetism as well as superparamagnetism below 90K [221]. It has already been discussed earlier that the Zn^{2+} ion is substituted by Ni^{2+} ion in tetrahedral coordination for $x = 0.03$ while with $x \geq 0.06$, in addition to the tetrahedrally coordinated Ni^{2+} ion, the ion also exist in octahedral coordination in the secondary NiO phase which increases with increase in Ni content in the compound. Here it is worth mentioning that Ni^{2+} ion consisting tetrahedral and octahedral coordination possesses effective magnetic moment with 2.83μ_B and that NiO nanoparticles explore antiferromagnetic nature at higher temperature and at low temperature explore superparamagnetism/spin glass like property. It has been reported that Ni-doped ZnO nanoparticles within the soluble limit ($x < 0.06$) show room temperature ferromagnetism and various reasons have been predicted for such magnetic property in the compound. One such theory is attributed to the creation of BMP [200, 222], wherein the localized spins of incorporated ion interact with the charge carriers such as oxygen vacancies and affect magnetic polarization of the nearby local moments. In $Zn_{1-x}Ni_xO$ nanopowders with $x \geq 0.06$, the observed weak ferromagnetic properties at low temperature shown in figure 3.12 seems to be the mutual effect of the interaction with Ni^{2+} spin at the tetrahedral sites and charge carriers such as V_O in originating BMP and the overlapping superparamagnetism of the secondary NiO phase.

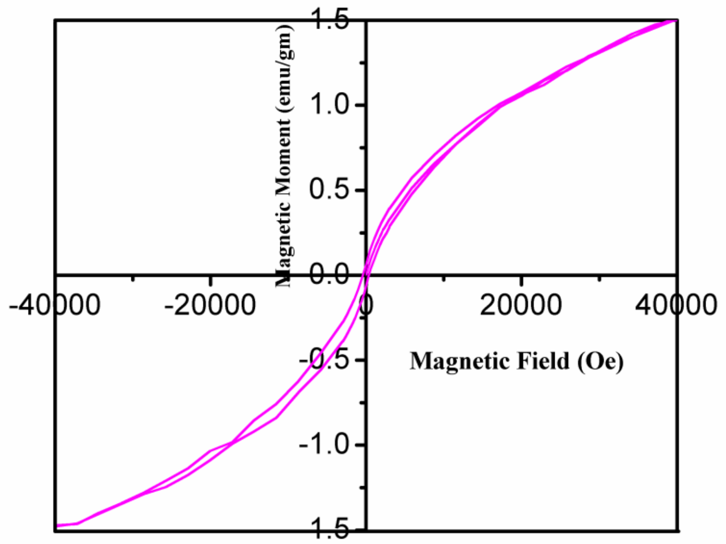

Fig. 3.12. M-H loop of $Zn_{0.91}Ni_{0.09}O$ sample by SQUID.

3.3.9. ME coupling:

To investigate the interplay between charge carriers and spin ordering, the variation of room temperature ME voltage coefficient as function of magnetic field has been studied for two samples $Zn_{0.91}Ni_{0.09}O$ and $Zn_{0.85}Ni_{0.15}O$. The results are presented in figure 3.13. The electric and magnetic poling is conducted on the samples for dipole ordering before the measurement of ME coefficient [185]. The ME coefficient (α_E) is measured through a dynamic technique wherein an ac and a dc magnetic field is applied simultaneously [186]. The sample was positioned in ME as discussed in sec. 2.2.8. ME voltage coefficient, can be calculated from the relation [188, 189]

$$\alpha_E = \left(\frac{dE}{dH}\right)_{H=0} = \frac{V}{h_0 d} \tag{3.2}$$

The curves in figure 3.13 are observed a good fit to fifth order polynomial. The ME voltage coefficient (α_E) for the compound with x = 0.09 is obtained as 1.04 mV/(cm Oe) at zero magnetic field. The second, third and fourth order coefficient (β, γ, δ) were found to be 3.60×10^{-6}, 2.00×10^{-9} and 1.32×10^{-13} (in appropriate units) respectively. The compound with x = 0.15 exhibit slightly higher ME coefficient (with α_E = 1.147) than that of the compound with x = 0.09. The dominant impact thus originates due to the linear term in H in the power series expansion and therefore will be suitable in manipulating this feature in ME coupling devices stand on these nanocompounds.

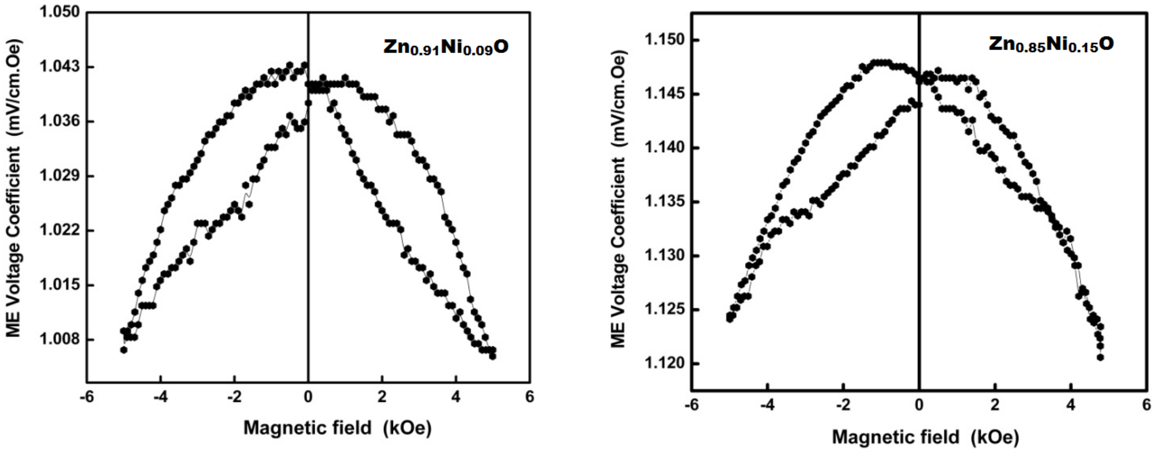

Fig. 3.13. Variation of ME voltage coefficient with DC magnetic field of $Zn_{0.91}Ni_{0.09}O$ and $Zn_{0.85}Ni_{0.15}O$ samples.

3.4. Conclusions:

The pure and doped $Zn_{1-x}Ni_xO$ nanoparticles have been effectively synthesized through chemical precipitation method. XRD characterization endorses the replacement of relatively small size Ni^{2+} ion with tetrahedral coordination at the Zn^{2+} sites of host lattice in the compound for $x = 0.03$. A secondary phase due to octahedral NiO arises in the nanoparticles with $x \geq 0.06$ in addition to the dominant wurtzite phase of ZnO. The crystallite size of the nanoparticles acquired from XRD recordings agrees well with the grain size obtained from the TEM photograph thus approving single domain in the grain. The HRTEM images have projected the [101] as the favored direction of crystal growth for the compounds. The UV-Vis spectra explore a blue shift in the absorption peak of Ni-modified ZnO nanoparticles with respect to pure ZnO. Five Gaussian like peaks relates to different emission centers are exhibited in the FL spectra for all prepared Ni-modified ZnO nanopowders. The peaks have been found to be slightly shifted towards lower wavelength in the Ni-doped ZnO nanopowders. The dielectric constant decreases with increasing the concentration of Ni in host lattice instead of increasing value as the polarization contribution originates from both bulk and grain boundary effect in the doped samples. The SQUID study exhibit weak ferromagnetism in the Ni-doped ZnO samples. The magnetic behavior of the samples can be understood in terms of BMP created in the wurtzite crystal phase and the superparamagnetism with secondary NiO phase. The ferroelectric and ferromagnetic nature of Ni-doped ZnO nanoparticles make these compounds enable for reliable multiferroic device applications. The ME characteristic explores strong first order coupling of electric and magnetic field which will come helpful in exploiting this aspect for devices.

(Results of this work have been published in Journal of Alloys and Compounds, 730 (2018) 399-407)